LAWRENCE
LIVERMORE
NATIONAL
LABORATORY

LLNL-BOOK-765159

# Resonance ionization mass spectrometry (RIMS): Fundamentals and applications including secondary neutral mass spectrometry

M. R. Savina, R. G. Trappitsch

January 8, 2019

Photoionisation and Photo-induced Processes in Mass Spectrometry

## Disclaimer

# Resonance ionization mass spectrometry (RIMS): Fundamentals and applications including secondary neutral mass spectrometry

Michael R. Savina, Reto Trappitsch

Lawrence Livermore National Laboratory

## Introduction

Resonance Ionization Mass Spectrometry (RIMS) is elementally selective ionization of atoms followed by mass analysis. Like some other forms of postionization mass spectrometry, RIMS exploits the fact that the majority of atoms sputtered or vaporized from a solid are neutral and therefore large gains in detection efficiency can be made by detecting the neutral rather than ionic fraction. Thus, RIMS is used in challenging analytical applications such as ultra-trace analysis of solid materials such as cosmochemical and environmental samples. Because the atomization and ionization events are separate, RIMS can be used to study sputtering phenomena such as angular and velocity distributions, ion-induced surface modifications, and energy partitioning among excited states in sputtered neutrals. It is also used for basic spectroscopic studies such as discovering new atomic energy levels, precise measurement of ionization potentials, and assigning isotope shifts and hyperfine splittings.

The advent of tunable lasers provides high intensity beams of precisely specified wavelengths and allows RIMS to achieve its unique combination of high selectivity and high ionization efficiency. Lasers tuned to precise transition energies excite the atom of interest via one or more bound electronic excited states until its total energy exceeds its ionization potential. Because atomic transition lines are narrow compared to the spacing between them, and continuum absorption of photons between discrete transitions is orders of magnitude lower than even a moderately strong electronic resonance, unintended off-resonant ionization of other elements is greatly suppressed. Further, the efficiency of resonant ionization of atoms with even modest laser power can approach 100%. Thus, RIMS excels in analyses in which one must discriminate against isobaric interference and/or the number of atoms of the element of interest in the sample is small.

Figure 1 shows a schematic of a simple RIMS system, in this case a sputtered neutral mass spectrometer based on reflectron time-of-flight (ToF) spectrometer. A portion of a solid sample is vaporized by a pulsed ion beam. The liberated material consists of atoms and molecules, both as neutrals and ions. Whereas sputtered ions are the detected species in Secondary Ion Mass

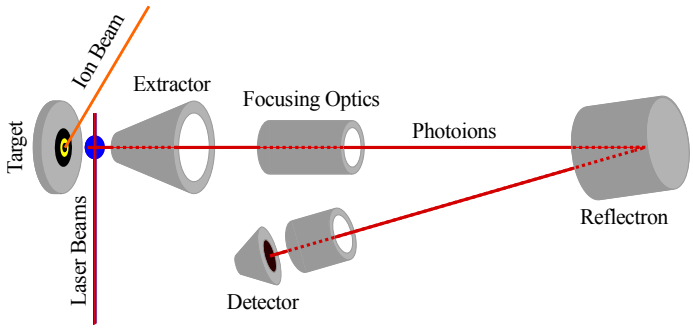


Figure 1: Schematic diagram of a RIMS reflectron time-of-flight mass spectrometer.

Spectrometry (SIMS), in RIMS they are usually swept away by an electric field and one or more pulsed lasers tuned to specific resonances in the element of interest are passed through the remaining neutral cloud to affect efficient ionization of that element, while other elements and molecules are largely unaffected. The photoions are then extracted into the ToF mass analyzer. Since resonance ionization produces only singly-charged ions, the mass spectrum is easily interpreted as the isotopes of the element of interest. In some cases, molecular interference occurs due to resonantly enhanced multiphoton ionization (REMPI) of molecules, whose resonances can be numerous and broad, however one of the unique features of RIMS is the ability to extinguish the resonant atomic signal by a slight detuning of one of the lasers. This uncovers all sources of background (dark counts, unsuppressed secondary ions, non-resonantly ionized atoms of other elements, photofragments, and REMPI molecular ions) and allows for a quantitative background correction.

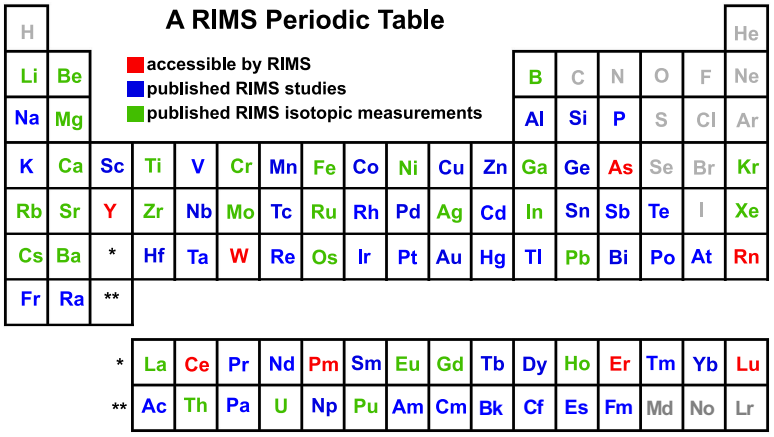


Figure 2: Periodic table showing elements that either have been or could reasonably be analyzed by RIMS. References to the large number of resonance ionization schemes on which this figure is based are given in the Resources section at the end of the chapter.

Figure 2 is a periodic table of elements that either have been or could be ionized by RIMS using common tunable lasers. Nearly all elements have been analyzed; those that are not accessible (most halogens and the upper right corner of the periodic table) either have very high ionization potentials or very high first excited states, such that vacuum ultraviolet (VUV) photons or multi-photon transitions are required. While VUV or two-photon excitation do produce viable resonance ionization schemes in some cases, they are generally restricted to noble gas analysis due to the high backgrounds they produce when applied to sputtered neutrals.

In this chapter we discuss the important considerations in choosing resonance ionization spectroscopy (RIS) schemes, lasers, and mass analyzers, and applications of the RIMS method to various challenging analyses.

# Resonance Ionization Fundamentals

## Laser Spectroscopy

The interaction of gas-phase atoms with laser photons forms the basis of RIMS. Figure 3a shows a simple generic RIS scheme involving two lasers. Photons with a wavelength $\lambda_1$ from the first laser excite an atom from its ground state to a bound electronic state. Absorption of a photon ($\lambda_2$) from the second laser excites the atom above its ionization potential, where it undergoes electron emission and forms an ion.

A simple calculation illustrates the feasibility of laser resonant excitation of atoms. The absorption cross section of a strong bound-bound transition is of order $\lambda^2$ (Hilborn 1982), so that the cross section, $\sigma$, of a transition in the visible (400 – 800 nm) is ~$10^{-9}$ $cm^2$. The lifetime, $\tau$, of the upper state of such a transition is of order 10 ns. Therefore, the photon flux required to achieve a transition probability of one is $1/\tau \times 1/\sigma$ = ~$10^{17}$ photons/$cm^2$/sec. For a laser with a temporal pulse width of 10 ns this corresponds to an intensity of a few mW/$cm^2$ over the visible range. In practice, effects such as Doppler and power broadening and laser spectral bandwidth increase the required power to a few tens to perhaps 100 mW, but this is still easily obtained in tunable lasers. Cross sections for transitions are often not tabulated, but can be estimated from Einstein A coefficients, which are tabulated for many transitions (Sansonetti and Martin 2005).

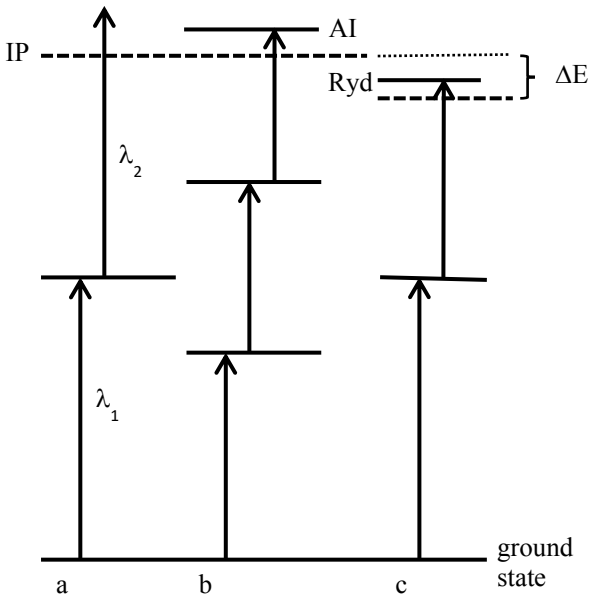


Figure 3: Generic RIS schemes. A) Two-photon excitation of an atom from the ground state to the ionization continuum. B) Three-photon scheme terminating on an autoionizing state (AI). C) Two-photon scheme terminating on a Rydberg state (Ryd) with the ionization potential (IP) lowered by an amount ΔE by an external field.

The ionizing transition is generally far weaker than bound-bound transitions. Cross sections for transitions into the ionization continuum (such as depicted in Figure 3a) can be of order $10^{-17}$ $cm^2$. Where possible, one uses transitions to autoionizing (Figure 3b) or Rydberg states (Figure 3c). Ionization from Rydberg and AI states is often 2-3 orders of magnitude more efficient than non-resonant ionization as in Figure 3a, but this still requires an intense, usually pulsed, laser. Very often, the ionizing transition is not saturated.

The concept of saturation is commonly understood to mean the point at which negligible signal is generated by increasing the laser power, and is reasonably well described by an exponential equation:

$$N_i = N_a \left(1 - e^{-I/I_{sat}}\right) \qquad (1)$$

where $N_i$ is the number of ions created, $N_a$ is the number of available atoms, $I$ is the laser irradiance and $I_{sat}$ is the saturation irradiance. (Note that the "saturation irradiance" corresponds to an ionization efficiency of ~63%.) The general form of Equation 1 holds for incoherent excitation of a two-level system in which the laser pulse length is much longer than the natural lifetime of the upper state (Letokhov 1987). Pulsed lasers are broadband compared to the linewidth of an atomic transition and therefore induce incoherent excitation, but they have pulse lengths on the order of the natural lifetime of the transition or less. However, since the upper state population in a RIS scheme is rapidly removed by the second laser, the effective lifetime of the excited state is cut short and Equation 1 is a reasonable approximation. Similarly, continuous wave lasers are

generally narrowband and would be expected to produce coherent excitation, however the perturbation of the upper state by the second laser in the scheme serves to interrupt the coherence of the process as a whole, such that Equation 1 is a reasonable approximation to the behavior.

One commonly constructs saturation curves (ion signal vs. laser intensity) and fits Equation 1 to estimate the efficiency of a RIS scheme, and to determine the optimal laser power for each transition. It is in fact detrimental to increase the laser power to more than a few times the saturation irradiance (corresponding to ~95% of the maximum signal in Equation 1) since the extra photons increase non-resonant background without contributing significant extra signal.

Figure 3 shows three different RIS schemes illustrative of most common RIMS methods. The first (1a) is a two-photon scheme from the ground state to the ionization continuum via a resonant intermediate. The second photon in this scheme can be a different wavelength than the first, and indeed since the non-resonant ionization step requires very high power this is often a fixed-frequency laser such as a Nd:YAG (either fundamental or harmonics depending on the minimum required photon energy), which can have much more power than a tunable laser. This is referred to as a two-photon two-color RIS scheme. Alternatively, the second photon can be the same as the first, in which case the scheme is two-photon one-color. One-color schemes, which can require more than two photons, are obviously simpler and cheaper than multi-color schemes and many are known, especially for heavy elements such as REEs (Young, Donohue et al. 1989) and actinides (Donohue, Young et al. 1985). One-color schemes are rarely efficient since the ionization step is generally non-resonant. They are also prone to increased backgrounds since in order to reach the IP with two photons the laser wavelength is typically in the ultraviolet where many molecules absorb. Because the ionization step is inefficient the laser power must be high, which also promotes non-resonant ionization photofragmentation of molecules.

Figure 3b is a three-color scheme terminating on an autoionizing (AI) state. A three-color scheme will typically be more selective than a two-color scheme since the energy of each photon is lower, thereby helping to suppress non-resonant ionization of unwanted species. In addition, less laser power is required since the cross sections are generally higher for lower energy transitions. Of course, two-color and one-color schemes can also terminate on AI states. Autoionizing states are metastable states above the ionization potential that decay via electron emission much faster than via photon emission, and transitions to them can have cross sections much higher than transitions to the continuum. Because AI states are short-lived, transitions to them are usually much broader in wavelength than bound-bound transitions, and so less precision and stability is required of the laser.

In Figure 3c, the last transition is to a Rydberg state below the ionization potential of the atom. In this case, the ion extraction field of the mass spectrometer lowers the effective IP such that high-lying Rydberg states are unbound. To first order, an external electric field gradient lowers the effective IP according to $\Delta E = 2\sqrt{F}$ in atomic units (Littman, Kash et al. 1978), which corresponds to $\Delta E = 6.1\sqrt{F}$, where $\Delta E$ is the change in IP in $cm^{-1}$ and $F$ is the field gradient in V/cm. A $\Delta E$ of >100 $cm^{-1}$ is easily achieved in most mass spectrometers.

Figure 3 is a simplified version of a RIS scheme since it neglects isotope shifts. The isotopes of an element each have their own unique electron energy levels and thus each has its own unique

transition energies. The difference in energy between two isotopes undergoing the same electronic transition is known as the transition isotope shift. For light elements the difference is mainly due to the mass difference between the two nuclei, while for heavy elements it is mainly due to differences in the charge distribution of the nuclei. The effects are most pronounced for the heaviest and lightest elements. Isotope shifts for the intermediate mass elements Ne through Ba are less than 3 GHz, and usually less than 1 GHz (Stern and Snavely 1976). Isotope shifts are important for REE and actinide RIMS, where they often exceed 10 GHz and can lead to poor ionization efficiency and isotopic fractionation if the bandwidth of the laser is insufficient to cover the shift. Large isotope shifts also increase the necessity for laser stability, since a drift in wavelength can favor one isotope over another (Isselhardt, Savina et al. 2011).

## Selection rules

Since RIMS relies on the sequential excitation of atoms, it is dependent on atomic selection rules. The most important of these are total angular momentum and parity, which are rigidly observed for all atoms. The total angular momentum, $J$, of an atom is the vector sum of the total orbital (L) and spin (S) angular momenta of the electrons:

$$\vec{J} = \vec{L} + \vec{S} \qquad (2)$$

Since closed electronic shells do not contribute to orbital or spin momentum it is sufficient to consider only valence electrons in Equation 2. The atomic states of atoms are expressed in term symbol notation:

$$^{2S+1}L_J$$

where $2S+1$ is the spin multiplicity. The allowedness of a transition can thus be gauged by simply inspecting the term symbol. The $J$ states range from $|L - S|$ to $L + S$. (Note that for $L \geq S$, the number of $J$ states is simply equal to the spin multiplicity.) The angular momentum selection rule for an atomic transition is $\Delta J = 0, \pm 1$ for unpolarized light, with the caveat that $J=0 \leftrightarrow J=0$ is forbidden for linearly laser polarized light commonly used in RIMS.

Parity arises from the orbital angular momentum, and is defined as

$$p = -1^{\Sigma l_i} \qquad (3)$$

where the $l_i$ are the orbital angular momentum quantum numbers of the valence electrons of the atomic state. Parity can take only two values, namely ±1, and the two states are referred to simply as even and odd. The selection rule is $\Delta p \neq 0$, *i.e.* transitions are allowed only between states with different parity. Equation 4 reduces to $p = -1^L$ for atomic states with exactly one valence electron, which gives rise to the selection rule $\Delta L = \pm 1$ for transitions between states that preserve the single valence electron. Atoms with multiple valence electrons have no $\Delta L$ selection rule. Indeed $\Delta L = 0$ transitions are often strong in complex atoms. Parity and $J$-values for atomic states are usually listed in tables of atomic energy levels, however term symbols are generally not known for all atomic states, particularly the higher states of complex atoms. Fortunately $p$ and $J$ are sufficient to determine the allowedness of a proposed transition, though not its cross section.

Additional selection rules come into play regarding the accessibility of electrons for excitation *within* a $J$ state. The $J$-value of an atomic state is composed of $2J+1$ energetically degenerate sub-

states $m_J$, with quantum numbers ranging from -$J$ to $J$ (-$J$, -$J$+1, …, $J$). For linearly polarized light, a transition between atomic states is actually a number of transitions between $m_J$ sub-states having the selection rule $\Delta m_J = 0$, with the caveat that $m_J = 0 \leftrightarrow m_J = 0$ is forbidden when $\Delta J = 0$. The change in degeneracy between two states limits the achievable ionization efficiency when $\Delta J = 0$ or -1, which leads to the important rule of thumb that efficient RIS schemes have $\Delta J = +1$ for all transitions. Figure 4 illustrates all three cases of the $\Delta J$ selection rule. Transition A has $\Delta J = +1$, and all of the electrons in the ground state are involved. This can theoretically lead to 100% ionization in a fully saturated RIS scheme (assuming the other transitions are also $\Delta J = +1$). Transition B has $\Delta J = 0$ and has a maximum theoretical ionization efficiency of 66% since 1/3 of the ground state electrons are inaccessible. Transition C has $\Delta J = -1$ and has a maximum theoretical ionization efficiency of 60% since 40% of the ground state electrons are inaccessible. These effects can be avoided with unpolarized light, which has different $m_J$ selection rules, however the added complication of de-polarizing the laser is generally not necessary if one chooses a RIS scheme wisely or simply understands and accepts the limitations.

Other selection rules are less rigorous, especially in high $Z$ atoms with many electrons and significant configuration mixing such as REEs and actinides. The spin multiplicity rule $\Delta S = 0$ is broken, though $\Delta S \neq 0$ transitions are generally weaker than $\Delta S = 0$. For atoms with single valence electrons one observes transitions involving only single electrons, however this is not the case for atoms with multiple valence electrons due to configuration mixing. States in such atoms are often not pure and can be regarded as combinations of states. This leads to transitions between states that would otherwise be forbidden. Since the allowedness comes from only a portion of the states involved, the transitions are not as strong as those between pure states but can still be significant. This can be a boon or a burden. The large density of states and relaxed selection rules lead to a large number of allowed transitions from which to construct a RIS scheme (the Palmer Atlas (Palmer, Keller et al. 1980) lists over 5,000 uranium transition lines between 380 and 900 nm). However, it can also lead to significant off-resonant ionization of unwanted elements either through accidental resonances (*i.e.* unintentional excitation via a resonant or near-resonant process) or more commonly through continuum absorption since the continuum is made up of the sum of the Lorentzian tails of the many atomic states.

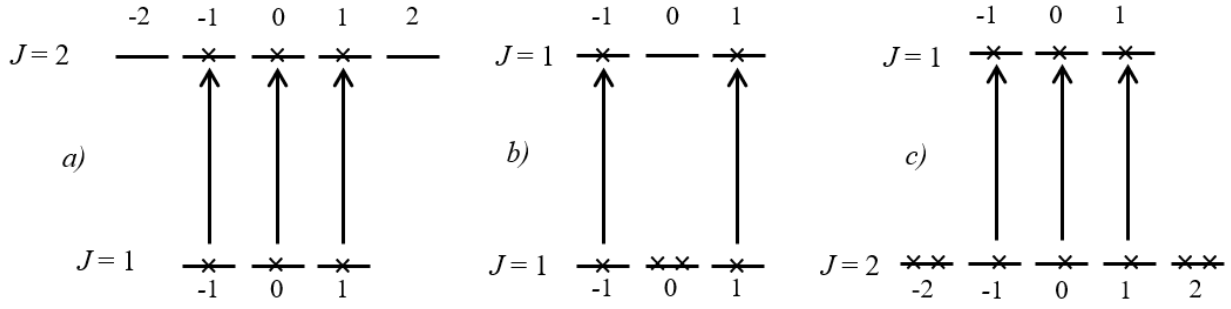


Figure 4: Allowed transitions and population distributions at equilibrium for a) $\Delta J = +1$, b) $\Delta J = 0$, and c) $\Delta J = -1$.

## Odd – Even effect

There is an additional complication when odd isotopes are present. The non-zero spin $I$ of the odd nucleus couples to the angular momentum states $J$ and gives rise to non-degenerate magnetic states $F$ ranging over $F = |J - I|, |J - I + 1|, \ldots J + I$. The $F$ states have degenerate substates $m_F$, which are analogous to the $m_J$ substates. The selection rules are $\Delta F = 0,\pm1$, $\Delta m_F = 0$. Because $I$ is half-integral, there is no forbidden $F=0 \leftrightarrow F=0$ transition as there is in even isotopes, and no forbidden $m_F=0 \leftrightarrow m_F=0$ transition. Thus, unlike in even isotopes, 100% ionization is possible in $\Delta J$=0 transitions. This leads to isotopic fractionation favoring odd isotopes in the RIMS spectrum, since as we have seen the maximum possible ionization efficiency for an even isotope is less than 100% when $\Delta J$=0 transitions are included in the RIS scheme. In fact, it is possible to design RIS schemes that ionize *only* odd isotopes. Figure 5 shows a Gd RIS scheme in which the first transition is $\Delta J$=0, and the others are $\Delta J$=-1. By excluding the $m_J$=0 ↔ $m_J$=0 transition in the first step and weeding out the other $m_J$ levels as the degeneracy decreases, no electron in the ground state has a path to ionization. In contrast, most of the $m_F$ levels of the ground state are connected to the autoionizing state. The RIMS spectrum contains only $^{155}$Gd and $^{157}$Gd, with no peaks at the two major isotopes $^{156}$Gd and $^{158}$Gd (Niki, Motoki et al. 2006).

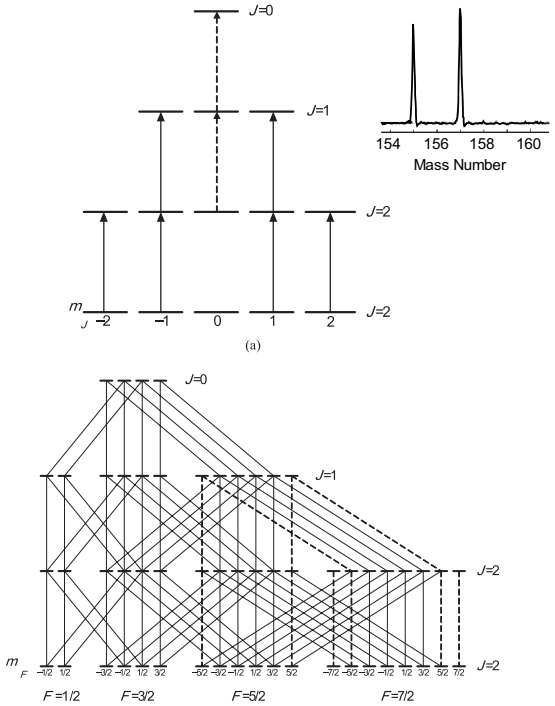


Figure 5: Gd RIS scheme in which no even isotopes (upper) are ionized. Odd isotopes (lower) have multiple paths to ionization. Solid lines indicate allowed transitions, dashed lines indicate forbidden transitions. The RIMS spectrum is at upper right. From (Niki, Motoki et al. 2006)

Further, odd isotopes ionize at a faster rate than even isotopes. Figure 6 shows a $J$=0↔$J$=1 transition in an odd isotope with $I$=1/2. Each $m_F$ sub-state of the lower state is connected to two $m_F$ sub-states in the upper state, and the laser acts to equalize the population across each connected pair. This leads to an upper state population at saturation of 66%, rather than the 50% maximum in the corresponding even isotope. The larger number of pathways available to ionize an odd isotope leads to a greater ionization rate. The difference is most apparent in unsaturated RIS schemes where 100% ionization is not achieved (Wunderlich, Hutcheon et al. 1992). Even in apparently saturated schemes, atoms in the low-intensity wings of the laser profile will not reach 100% ionization and so odd isotopes will reach higher ionization efficiency than the corresponding even isotopes, leading to some isotopic fraction.

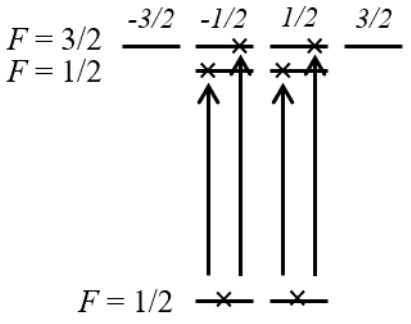


Figure 6: Hyperfine splitting and allowed transitions between $J$ = 0 and $J$=1 levels in an atom with nuclear spin $I$ = 1/2.

The other important odd-even effect is hyperfine splitting. As seen in Figure 6, the nuclear magnetic coupling creates non-degenerate *F* states, resulting in an apparent broadening of the odd isotope transition. This may have consequences for a laser with limited bandwidth that fails to excite all the transitions within the hyperfine envelope.

As in any mass spectrometric analysis of isotopic compositions, it is important to correct spectra with certified standards. All mass spectrometers fractionate isotopes and all must use standards, however the added spectroscopic fractions possible in RIMS (isotope shift, odd-even effect) make standards extra important. Careful use of standards, including before-and-after measurements (i.e. bracketing) allows RIMS to make accurate isotopic measurements (Savina, Isselhardt et al. 2017).

# Reduction to Practice

## Laser selection

The choice of laser systems for a RIMS instrument depends on the application. In general, analytical RIMS is used for isotope ratio measurements or for trace elemental or isotopic analysis. When the number of analyte atoms in a sample is low the useful yield (defined as the number ions detected divided by the number consumed) must be maximized, and so high ionization efficiency and therefore pulsed lasers are required. When the *concentration* of analyte atoms is low and the ability to discriminate against isobars and backgrounds is important, continuous-wave (cw) lasers are often used. When a precise isotope ratio measurement is required the laser bandwidth must be wide enough to cover the isotope shift of the element in question, and there should ideally be enough power across the bandwidth to saturate all the isotopic transitions to avoid fractionation. Excess bandwidth is undesirable since it wastes power and the non-resonant photons can cause backgrounds; a 10 GHz bandwidth is enough to avoid most fractionation effects even in REEs and actinides. When a single isotope must be detected with high selectivity, narrow bandwidth (generally cw) lasers are required.

The most common tunable pulsed lasers for RIMS are dye and Ti:Sapphire. The high instantaneous power (i.e. high photon flux during the pulse) and broad, tunable bandwidth of pulsed lasers make them suitable for isotopic analysis where it is important to cover the isotope shift to avoid spectroscopic fractionation. Dye lasers often have high pulse energies (>100 mJ / pulse at some wavelengths) but are generally restricted to pulse repetition rates of 100 Hz or less, which can lead to long analysis times. Ti:Sapphire lasers have less energy per pulse (≤ 2 mJ in the fundamental, less in the harmonics) but can operate in the 1-10 kHz range. Dye lasers require solvents and periodic changing of the organic dyes, while Ti:Sapphire lasers are solid state. One important difference is that dye lasers and their harmonics cover a broad wavelength range from the UV to the visible continuously, while Ti:Sapphire lasers have gaps. The reason for this is that the fundamental region of the Ti:Sapphire laser is from ~700-1000 nm. Thus, the second harmonic region is from 350 to 500 nm and the third harmonic region is 233 to 333 nm. Despite the gaps and the lower power, Ti:Sapphire lasers are used in many RIMS instruments due to the higher repetition rate and ease of use.

Pulsed Optical Parametric Oscillators (OPOs) can also be used, however most have bandwidths much too large for RIMS. Many OPOs have pulse lengths of a few picoseconds or less and therefore have bandwidths of 50 GHz or more[1]. Since the vast majority of optical transitions have isotopes shifts of 10 GHz or less, the extra bandwidth represents wasted photons which can induce non-resonant background. Nanosecond OPOs with bandwidths of order 10 GHz are available, but are limited to 10-20 Hz repetition rate.

Continuous wave lasers, including dye and Ti:Sapphire versions but also diode lasers, are used for applications such as high dynamic range or high abundance sensitivity measurements. The lower irradiance of a cw laser makes it harder to saturate transitions, especially the ionizing transition, resulting in lower ionization efficiency compared to a pulsed laser with the same average power. The narrow bandwidth of cw lasers (often <1 MHz) allows for the excitation and ionization of single isotopes via the isotope shift. In fact cw RIMS is often used for high resolution laser spectroscopy. Highly accurate isotope shifts and hyperfine splittings can be measured in this way (Schumann, Wendt et al. 2005). While the ion yield is generally lower than with pulsed lasers due to the lower instantaneous photon flux (in fact laser power is sometimes intentionally kept low to avoid power broadening the transitions), backgrounds can be much lower. Discrimination against other isotopes of the same element can exceed $10^{10}$ (Bushaw and Cannon 1997), and measurement of isotope ratios of order $10^{11}$ have been demonstrated (Geppert, Müller et al. 2005).

## Mass spectrometer considerations

As with any scientific instrument, the choice of the mass spectrometer for a RIMS system is informed by the intended use. A variety of mass spectrometers, most commonly quadrupole and ToF, can and have performed well in RIMS. Commercial systems can be adapted by adding a laser system (Franzmann, Bosco et al. 2018), or the mass spectrometer can be designed around the laser as an ion source (Veryovkin, Calaway et al. 2004).

For systems in which the sample is vaporized by simple heating, the choice of mass spectrometer is limited only by the ability to introduce the lasers. Quadrupole, ToF and, less commonly, magnetic sector mass spectrometers have been used with thermal ion sources. The sample is deposited from solution either onto a filament or into a furnace. In order to avoid oxide formation and thereby assure that the vapor consists primarily of atoms the sample may be overcoated with a reducing metal such as Ti (Eichler, Hübener et al. 1997). Overcoating can also help to reduce the amount of thermal ionization by lowering the work function of the surface. The lasers may be introduced by simply passing them over a heated filament. More efficient ionization can be achieved by using a colinear geometry in which the laser beam is directed along the length of a tube furnace such that the vapor experiences a relatively long residence time in the resonance laser beams as it diffuses the length of the furnace toward the mass spectrometer extraction region. This lowers the saturation irradiance since each atom has many opportunities to interact with the laser photons, and allows the use of either continuous wave (Ziegler and Bushaw 2008) or high repetition rate lasers (~10 kHz) with relatively low energy per pulse (Liu, Baktash et al. 2006).

---

[1] The minimum bandwidth of a pulsed laser is given by the time-bandwidth product, which cannot be less than 0.44 for a Gaussian temporal profile. A 10 ps pulse therefore has a theoretical minimum bandwidth of 44 GHz. In practice, the time-bandwidth product of OPOs is >0.5.

There are addition considerations for Secondary Neutral Mass Spectrometry (SNMS) systems in which the sample is atomized by an ion beam or laser pulse, and so it is useful here to contrast laser photoions with secondary ions. Secondary ions are born in a plane at the sample surface. Because they are all born at the same potential (i.e. the target potential), the spread in energy is that given by the atomization process. Neutrals sputtered by an ion beam have an energy distribution described to first order by the simplest form of the Sigmund-Thompson distribution (Gnaser 1999, Veryovkin, Calaway et al. 2004):

$$\frac{\partial^3 Y}{\partial E \partial^2 \Omega} \propto \frac{E}{(E+U_b)^3} \cos\theta \qquad (4)$$

where $Y$ is the sputtering yield (atoms sputtered per primary ion), $E$ is the kinetic energy of a sputtered atom, $U_b$ is the surface binding energy of the atom (often approximated as the enthalpy of sublimation), and $\Omega$ is the solid angle around the angle of ejection $\theta$, which is taken as the angle between the ejected atom and the surface normal. Many materials deviate from this idealized behavior in practice, especially in the angular distribution, but it is helpful in illustrating a few basic principles. The most probable velocity is half of the surface binding energy, which is generally a few eV, and the large majority have energies below 50 eV. Because the energy spread is relatively small, SIMS instruments, especially magnetic sector mass spectrometers, often use high electric field gradients to ensure high ion extraction efficiency. In this way, even high-angle atoms have a relatively small velocity component orthogonal to the secondary ion flight path.

In contrast, RIMS photoions are born in a laser beam and thus acquire an additional energy spread corresponding to the extraction field gradient across the laser volume. Figure 7 (discussed in greater detail below) plots normalized number densities of sputtered atoms along the laser beam direction 300 ns after a 300 ns primary ion pulse for three different metals. Most neutrals are still within 1-2 mm of the surface after a reasonable delay. The inherent energy distribution of the sputtered neutrals partially compensates for this effect. The total energy of an ion is its energy due to sputtering (Equation 4) plus the energy it acquires from the extraction field. Since lower energy neutrals are closer to the sample surface when the lasers fire, their photoions will be born at a higher potential than higher energy neutrals. The amount of compensation depends on a number factors (the mass of the ion, the length of the primary ion pulse, the time delay between the primary ion pulse and the laser pulse, the

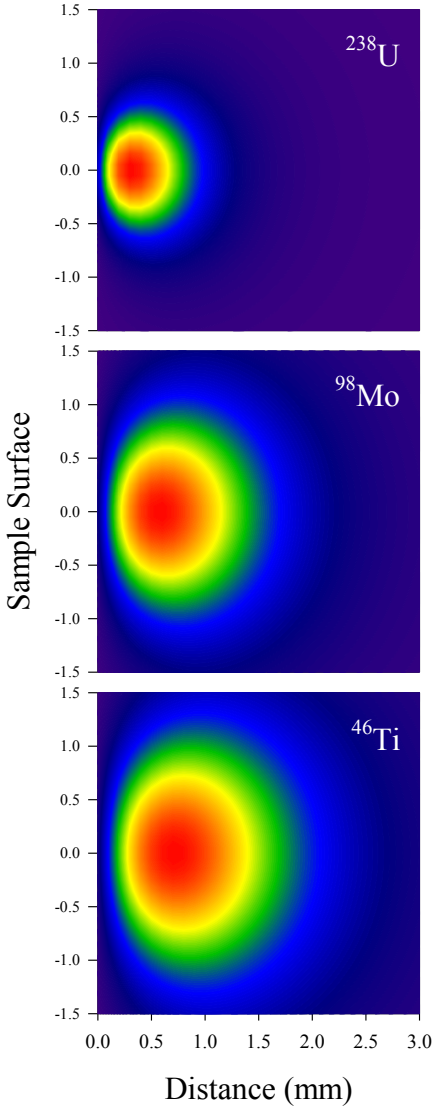


Figure 7: Normalized number density along the resonance laser direction of sputtered U, Mo, and Ti atoms above a solid surface 300 ns after a 300 ns primary ion pulse. Sample surface is at left (see Figure 1 for geometry).

diameter of the laser beam, the extraction potential, and the length of the extraction region) and must be modeled for each choice of parameters, however the energy spread of photoions is nearly always significantly greater than that of secondary ions. This can limit the transport efficiency of photoions compared to secondary ions unless the mass spectrometer design takes it into account (Veryovkin, Calaway et al. 2004), however the high ionization efficiency of RIMS compared to SIMS nearly always outweighs any ion transport differences.

In many cases the pulsed nature of most RIMS lasers makes time-of-flight a natural choice for the mass spectrometer. The photoion energy spread and the range of starting positions across the laser volume can degrade mass resolution in ToF instruments, since the range of energies and flight distances translate to a range of arrival times on the detector, however RIMS spectroscopic discrimination and the ability to quantify backgrounds reduces the need for high mass resolution and modest resolution is acceptable. A reflectron-type mass spectrometer is typically used to partially compensate for the energy and flight distance spread in the ions. Because the ionization region extends laterally up to several millimeters, RIMS ToF-MS systems often use cones rather than grids to extract ions into the drift region. The cone acts as an ion focusing optic and allows the extraction field to be shaped to accept ions born along the laser direction with a relatively high velocity perpendicular to the drift tube.

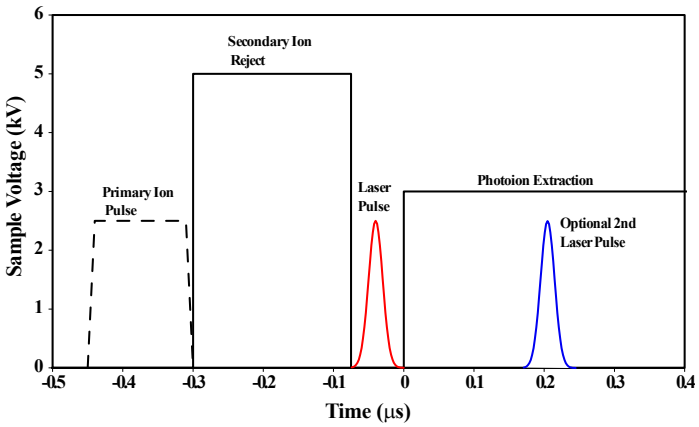


Figure 8: Sample pulsing scheme for secondary ion rejection in RIMS. The solid black line is the sample potential over time, the dotted line is the primary ion pulse, and the red and blue peaks represent resonance ionization laser pulses.

Since secondary ions are a source of backgrounds in sputtered neutral RIMS, they must be suppressed or ejected prior to resonance ionization. In a reflectron ToF instrument this can be accomplished by pulsing the sample bias. A typical pulse sequence is shown in Figure 8. With the sample bias set to zero, a primary ion beam is pulsed onto the sample, then the bias is raised to a potential above that of the reflectron. Secondary ions will not be turned by the reflectron and thus will not hit the detector. The bias is then lowered briefly to zero and the resonance lasers are pulsed to ionize the neutrals. This is often done to avoid Stark effects, however in most RIMS schemes this is unnecessary since the extraction field gradient is low and the Stark shift is negligible. The sample is then biased to the correct potential for the reflectron, and the photoions are accelerated into the mass spectrometer. Alternatively, one can bias the sample negatively during the primary ion pulse and for a few hundred nanoseconds afterwards to pull positive secondary ions back onto the sample, and then proceed with ionization and acceleration. In cases where the Stark shift is negligible, which are the vast majority, a second set of lasers tuned to a different element can be pulsed at some delay after the first (blue peak in Figure 8). This has the effect of delaying the start time for the second element and can be used to resolve isobaric interferences in the two elements. An example for the resolution of $^{58}$Fe / $^{58}$Ni is given in the discussion of applications below.

## Laser overlap

RIMS lasers should ideally generate enough intensity to saturate electronic transitions over an area large enough to overlap a significant fraction of the sputtered neutrals. For the first transition this can be a pulse energy as low as a few μJ, but for the higher and especially autoionizing transitions >1 mJ is often required. Because the vaporization and ionization events are separate, the method for accomplishing overlap depends on the method of atomization. For simple heating, the vapor is produced continuously, which makes the use of pulsed lasers problematic in a perpendicular geometry in which the lasers are parallel to the sample surface. A laser with a pulse length of 10 ns running at 1 kHz has a duty cycle of $10^{-5}$. Even low velocity atoms are moving too fast to remain in a 1 mm laser beam for more than a few microseconds, so each laser pulse irradiates a fresh batch of atoms. This means that only 0.001% of the vapor will be irradiated. For this reason, the colinear geometry discussed above is sometimes used. This geometry does not support thermal ion rejection; however the use of relatively low work function materials often keeps such ions at an acceptable level, and off-resonant background corrections can be made if necessary.

For direct solid sampling a perpendicular geometry is generally used. A pulsed ion beam or laser vaporizes material from a solid, and the vapor is then irradiated by pulsed resonance lasers. Figure 7 shows normalized number densities of atoms sputtered from U, Mo, and Ti metal surfaces 300 ns after a 300 ns primary ion pulse. The sputtered neutral plume can be considered of order mm in diameter, which is roughly the size of laser beams commonly used in RIMS. Thus the time required to generate a sputtered neutral (SN) plume amenable to RIMS is of order hundreds of nanoseconds. Since the ionization timescale is of order a few nanoseconds, the SN plume can be considered stationary to a good approximation and we can regard the laser as taking a snapshot of the plume. The signal observed can then be described by the SNMS equation:

$$S = YI\sigma T \qquad (5)$$

Where $S$ is the number of ions detected, $Y$ has the form given by Equation 4, $I$ is the primary ion dose, $\sigma$ is the ionization probability, and $T$ is the combined transport and ion detector efficiency of the mass spectrometer. For a derivation of the SNMS equation and a full treatment of the effects of a non-stationary plume see (Wucher 2013). For our purposes we note that the product $Y{\cdot}I$ determines the amount of material sputtered from the sample and $\sigma$ is the fraction of sputtered neutrals that are ionized by the lasers and includes the laser/plume overlap. Note that equation 4 gives the observed signal, not the useful yield, which is defined as the number of ions detected ($S$) divided by the number consumed ($Y{\cdot}I$). From equation 4, this is simply $\sigma T$. In practice neither $\sigma$ nor $T$ are directly measurable, so one measures the sputtering yield for a given material and then calculates the useful yield as

$$UY = \frac{S}{YI} \qquad (6)$$

Figure 7 shows the effect of atomic mass on the sputtered plume density near the target and illustrates how the laser/plume overlap changes as the atomic mass changes. Heavy atoms ($^{238}$U) have moved roughly half the distance of the lighter atoms ($^{46}$Ti), which constitute a much more diffuse cloud at this time delay after the ion pulse (300 ns). A Gaussian beam with a FWHM 1.5 mm overlaps 56% of the sputtered $^{238}$U, but only 29% of the $^{98}$Mo and 22% of the $^{46}$Ti at its 50%

power contour. Increasing the overlap of $^{46}$Ti to 56% to match U requires a beam with a FWHM of 3.4 mm; however simply expanding the beam by that amount would reduce its intensity by a factor of five with a concomitant slide down the saturation curve. Alternatively, one could reduce the time between the primary ion pulse and the laser pulse, but this decreases the efficiency of secondary ion rejection because there is less time to accelerate the secondary ions. Figure 7 thus demonstrates a fundamental trade-off in RIMS efficiency: expanding the laser beam to maximize the overlap with the sputtered neutral plume decreases the irradiance and therefore the saturation of the ionization process. This is not a problem for the first transition in most RIS schemes, which is typically quite strong and easily saturated, however the cross sections weaken for each successive transition and therefore higher irradiances are required. Even strong autoionizing resonances typically require 10-100× more power to saturate than a reasonable first transition from the ground state, and so large laser volumes can be problematic. Alternatively, the delay time between the primary ion and laser pulses can be shortened in order to intercept the plume before it has expanded too much, however this leaves less time for efficient secondary ion ejection. As always, a reasonable trade-off must be found.

# Applications

RIMS is a valuable technique for cases in which the isotopes of interest in a given sample are limited by one or more of the following factors: the amount of analyte small, the target element or isotope suffers significant isobaric interference, or the required dynamic range is high. In many applications, more than one of these factors is present and an analytical solution depends on the specific problem at hand.

The topics we will focus on are high sensitivity analysis with applications to actinides and trace analysis of environmental and biological samples, isotopic analysis of stardust grains, and studies of electronic processes occurring when atoms leave surfaces either by sublimation or ion beam sputtering. This is by no means a complete overview of RIMS applications, but rather focuses on a few highlights that demonstrate representative applications that take advantage of the unique properties of RIMS. We compare RIMS to other techniques where applicable.

## Useful yield and abundance sensitivity

While several mass spectrometric techniques exist for trace elemental and isotopic analysis, RIMS is unique in its ability to deliver very high useful yield and thus is applied to atom-limited analyses, i.e. analyses of samples where the number atoms of the element of interest is small. To achieve highest useful yield requires lasers that can saturate all transitions at high laser overlaps. For example, using pulsed lasers in SNMS a useful yield of 38% is possible for U (Savina, Isselhardt et al. 2017). This takes advantage of the high ionization efficiency and high overlap achievable between pulsed lasers and pulsed sputtered neutral clouds for the analysis of heavy elements as demonstrated in Figure 7. The attainable useful yield drops to 18% for Ti using the same technique, owing to the lower degree of overlap (Trappitsch, Savina et al. 2018). For comparison, SIMS useful yields for U and Ti are of 1-3% (Hervig, Mazdab et al. 2006, Ranebo, Hedberg et al. 2009).

For these types of analyses it is important to ensure that the sputtered flux consists primarily of atoms rather than molecules, which is the limiting factor in the analysis of actinides and other

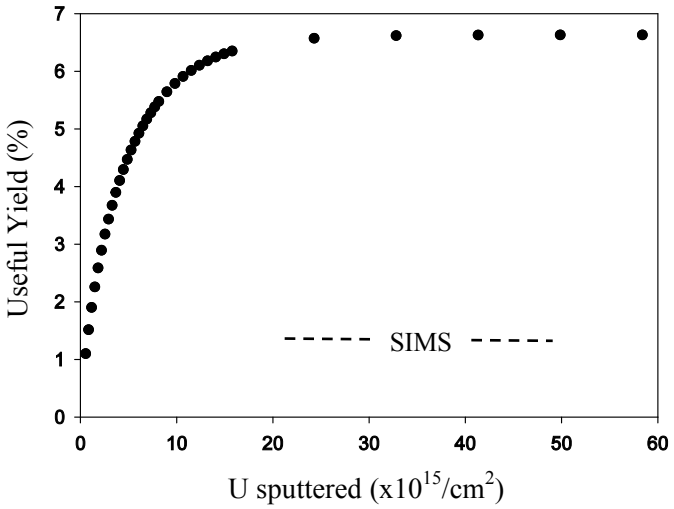


Figure 9: Useful yield for uranium sputtered from uranium oxide as function of the number of uranium atoms consumed by pre-sputtering with 3 keV $Ar^+$.

elements that form strong oxides that persist in the vapor phase after sputtering. The useful yields for Ti and U were achieved on cleaned, i.e., oxygen-free, surfaces and thus represent what one can expect for ideal samples. The surfaces were cleaned by pre-sputtering, which removes the oxide layer from the surface. This of course consumes part of the sample, which is not accounted for in the useful yield calculations and reduces the sample utilization efficiency. However, any sputtering-based surface analysis technique includes a surface cleaning step, and often further sputtering beyond simple cleaning is required to bring the surface into sputter equilibrium with the ion beam to achieve stable analysis conditions. For example, multi-component materials such as metal oxides undergo preferential sputtering of the lighter atomic component which persists until the surface composition has changed to the point where the absolute sputter rates of the two components are equal (Smentkowski 2000). The sputtering-induced surface damage will have accumulated such that the ratio of atoms to molecules in the sputtered flux is greatly increased. This has important consequences for RIMS, since it is the atomic fraction that is detected. Figure 9 shows the useful yield for the detection of uranium atoms sputtered from uranium dioxide as the surface is sputtered with 3keV $Ar^+$ ions. The surface concentration of U atoms is of order $10^{15}/cm^2$, so the surface has reached equilibrium with the ion beam after the removal of ~20 atomic layers. The useful yield is 6.5%, compared with 38% for the same analysis on a clean metallic surface, with the difference attributable to the fact that most of the sputtered flux consists of $UO_x$ molecules rather than U atoms. Even so, the RIMS useful yield surpasses that of SIMS for uranium dioxide (Ranebo, Hedberg et al. 2009) after the removal of only 2-3 atomic layers. Thus with minimal pre-sputtering amounting to the consumption of a few atomic layers, RIMS useful yields are several times higher than SIMS even on bulk oxides (Savina, Trappitsch et al. 2018).

An alternative reduction technique is to apply a reducing coating or sample backing. Overcoating with Ti, for example, raises the useful yield for metal oxides. The Ti coating reduces deposited oxides to their metallic states as they diffuse through under heating and allows them to come off the surface as atoms rather than oxides. A useful yield of $3\times10^{-5}$ for Pu can be obtained for a continuous heating method combined with a high repetition rate pulsed laser (6.5 kHz), which is already useful for environmental particles from Chernobyl and fallout in sediments from Pacific nuclear tests (Eichler, Hübener et al. 1997), as well as Pu fallout in seawater and Pu in dust particles from a nuclear fuel reprocessing plant (Trautmann and Wendt 2012). Using pulsed heating with pulsed laser ionization, a higher useful yield of $4\text{-}5\times10^{-3}$ can be achieved for Pu and Gd overcoated with Ti owing to the improved duty cycle as described in the laser overlap section above (Ofan, Ahmad et al. 2006). The duty cycle limitation for thermal sources can be overcome with a hot

cavity ion source, which confines the neutral atoms in a hot tube with a narrow exit aperture. Figure 10 gives a schematic diagram of a colinear RIMS system with a hot cavity ion source (Raeder, Hakimi et al. 2012). The mass spectrometer in this case is an orthogonal quadrupole, which prevents neutrals effusing from the source from hitting the detector. Using lasers with a repetition rate of 10 kHz a useful yield of $10^{-3}$ is achieved for Pu, with a limit of detection of $10^5$ atoms for single isotope detection. Because the mass spectrometer cannot measure all isotopes simultaneously the useful yield for elemental detection will be lower. The bottom panel of Figure 10 demonstrates the excellent discrimination between Pu, U, and Am for this system, as well as the low backgrounds. A similar colinear geometry with a magnetic sector mass analyzer has achieved a useful yield of 50-60% for Pd (Kron, Liu et al. 2016). The difference is likely due to a higher state of development of the latter instrument, as well as the lower loss of Pd atoms to oxide formation compared to Pu.

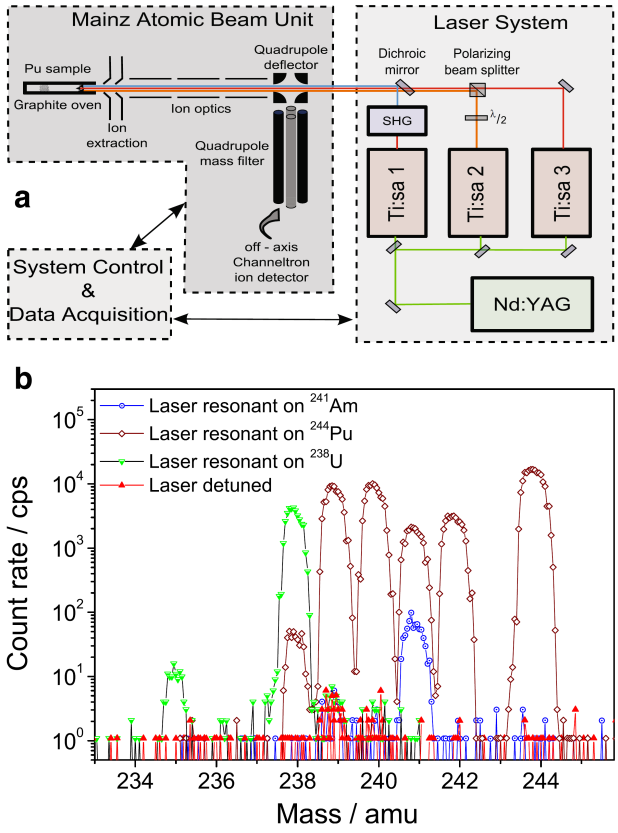


Figure 10: A colinear geometry RIMS system using a hot cavity ion source and high repetition rate lasers. From (Raeder, Hakimi et al. 2012).

Useful yield is only one figure of merit however; background suppression is also important. RIMS relies on selective ionization for background suppression, however this must be checked by acquiring off-resonance spectra. Provided the useful yield and selectivity for the application are sufficient, RIMS excels in ease of sample preparation (i.e. no chemical separations are necessary to remove isobaric elements) and the simplicity of the mass spectrometer itself. For example, the RIMS Pu useful yield using pulsed lasers is comparable to or better than AMS, which has a useful yield of ~$10^{-4}$ for Pu (Wallner, Faestermann et al. 2015). AMS has much lower backgrounds but greater complexity, so the analyst must decide which technique is most fit for a given purpose.

High background suppression in RIMS is achieved most readily with continuous wave lasers. The lower irradiance compared to pulsed lasers results in less off resonance ionization of atoms and molecules, and the narrow bandwidth allows for isotope-specific ionization, so that backgrounds caused by insufficient resolution in the mass spectrometer (peak tailing, for example) are greatly reduced. This comes at the cost of useful yield but can lead to high abundance sensitivity measurements. For example, three-color three-photon cw-RIMS using narrow bandwidth diode lasers enables isotope-specific detection of $^{158}$Gd at a rather high detection limit of 1.5 x $10^9$ atoms and an overall efficiency of only ~$10^{-7}$ (Blaum, Geppert et al. 2002). However,

the selectivity of $>10^7$ for $^{158}$Gd against other isotopes and the detection limit of <1 ppm in mouse tissue - comparable to ICP-MS - make the technique useful since there is essentially no sample preparation required and the mass spectrometer can be a simple quadrupole. An isotopic selectivity of $>10^{10}$ is possible for the radioisotope $^{90}$Sr is possible using cw-RIMS (Bushaw and Cannon 1997), and the same technique applied to $^{41}$Ca gives results approaching those attainable with accelerator mass spectrometry (AMS), which is usually used for high abundance sensitivity measurements, i.e. where the isotope ratio to be measured is extremely low. A $^{41}$Ca/$^{43}$Ca isotope ratio down to $\sim10^{-11}$ can be measured with RIMS, as compared to $\sim10^{-13}$ for AMS (Geppert, Müller et al. 2005). As in the case of the Pu analysis, AMS has a higher absolute abundance sensitivity but RIMS requires less sample and less sophisticated sample preparation and uses a simpler mass spectrometer. Thus RIMS has been used to study bone metabolism by tracking the amount of $^{41}$Ca excreted in the urine of human subjects who had been administered minute doses of the radionuclide (Denk, Hillegonds et al. 2006).

To conclude the discussion of useful yield, the RIMS instrument with highest known sensitivity is RELAX (Refrigerator Enhanced Laser Analyzer for Xenon) (Crowther, Mohapatra et al. 2008). Xenon gas is trapped on a cold finger and released by pulsed heating with an IR laser followed by pulsed resonance ionization and analysis in a ToF mass analyzer. The low desorption temperature assures that other atoms or molecules that could produce backgrounds in the Xe region are absent in the desorbed flux, and noble gas oxides are obviously not an issue. The RIS scheme is one-color three-photon, in which the transition to the first excited state requires two photons, followed by ionization via a photon from the same laser. A detection limit of ~950 atoms of $^{132}$Xe has been demonstrated for this instrument, which currently holds the sensitivity record for RIMS. Similar techniques have proven useful for analyzing Kr isotopes in meteorites (Strashnov and Gilmour 2014, Gilabert, Lavielle et al. 2016) and for detecting failed fuel elements in nuclear reactors via prior fuel pin tagging with Kr and Xe with unique isotope ratios (Iwata, Ito et al. 2014).

## Trace-element isotopic analyses of small samples

High sensitivity and selectivity make RIMS a valuable tool for *in situ* isotopic analyses of trace elements in small samples. While bulk techniques achieve higher precision, they often do not have the required sensitivity for analyzing small samples. RIMS is the method of choice when samples are small, chemical purification is not feasible, and isobaric interferences are present.

## Stardust grains

Elements heavier than hydrogen are created in stars by various processes collectively referred to as stellar nucleosynthesis (Burbidge, Burbidge et al. 1957). Certain primitive meteorites contain stardust grains, which are the only natural samples available to directly probe stellar nucleosynthesis and thus allow the possibility to study nuclear astrophysics in the lab. The best studied stardust phase is SiC, since these grains can be relatively easily separated from the host meteorite by chemical etching. Other types of grains, e.g., graphite and oxides have been studied as well, however our discussion here will focus on SiC. Silicon carbide stardust grains are generally less than 0.5 μm in diameter, however some range up to several μm, which makes them amenable to trace elemental analysis. The isotopic compositions of the major elements C and Si

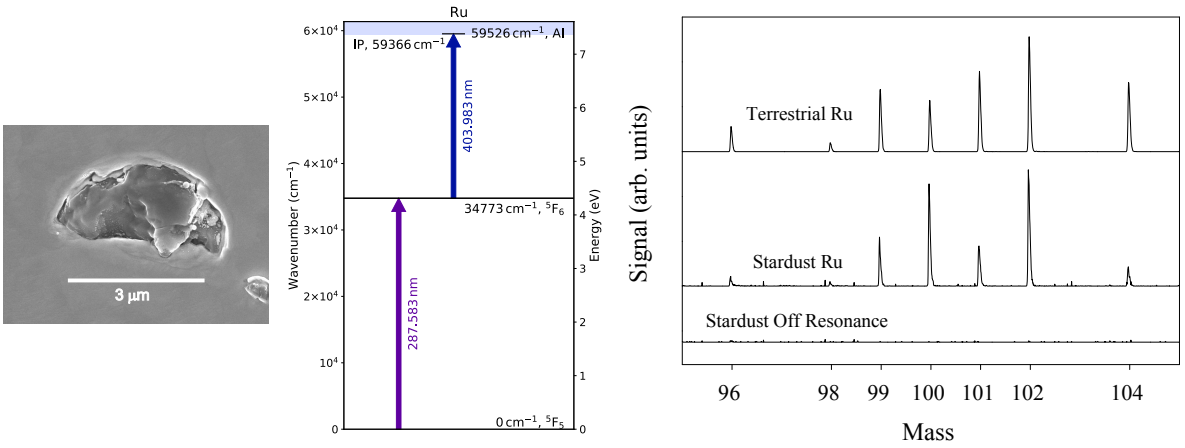


Figure 11: Left: Secondary electron image of a SiC stardust grain pressed into a gold substrate. Center: Ru two-color two-photon resonance ionization scheme. Right: RIMS spectra of terrestrial Ru metal (top), a SiC stardust grain (middle), and an off-resonance spectrum taken from the SiC stardust grain by detuning the first laser by 0.1 nm.

can be analyzed by SIMS, but RIMS is required to determine the isotopic composition of most other elements, some which contain a great deal of astrophysical information.

Elements heavier than Fe are formed in stars by neutron capture on seed nuclei, which competes with radioactive decay of unstable neutron-rich nuclei to determine the isotopic compositions of the elements that we observe today. The isotopic compositions of certain elements such as Zr, Mo, Ru, Sr, and Ba are diagnostic of particular nuclear processes in stars, and since each grain is a sample of a single star, the analysis of individual grains allows one to isolate particular processes. In contrast, terrestrial materials are a mixture of many astrophysical processes. Thus, determining the isotopic compositions of heavy elements in individual stardust grains allows stringent tests of particular stellar models. However, heavy elements are present in very low quantities in individual grains (typically of order $10^6$ atoms per grain) and suffer from isobaric interferences from neighboring elements. Therefore the study of individual grains requires both high useful yield and high elemental selectivity (Savina, Pellin et al. 2003).

RIMS analysis of stardust is done by dispersing the grains on a gold surface (Figure 11) and vaporizing them with a pulsed laser focused to a spot comparable to the size of the grain. Each pulse liberates a small amount of material, perhaps a few million atoms total. Several of these atoms are the element of interest, which is resonantly ionized by dye (Nicolussi, Pellin et al. 1998) or Ti:Sapphire (Savina, Pellin et al. 2003) lasers and detected by ToF-MS.

Figure 11 shows a SiC stardust grain (~3×2 μm) and the two-color two-photon RIS scheme used to analyze the grain's Ru isotopic composition. The Ru RIMS spectra of the grain and that of terrestrial Ru metal, both normalized to their $^{102}$Ru peaks, are also shown. The grain and metal have distinctly different spectra; the $^{96}$Ru, $^{98}$Ru, and $^{104}$Ru in the grain are strongly depleted with respect to $^{102}$Ru compared to the metal, and strong differences are evident in the other isotopes as well. The off-resonance spectrum taken on the stardust grain shows the lack of interference from the neighboring elements Zr, Mo, Rh, and Pd which all have isotopes in the Ru mass range, even though these elements are all present in the grain. The isotopic compositions of a collection of

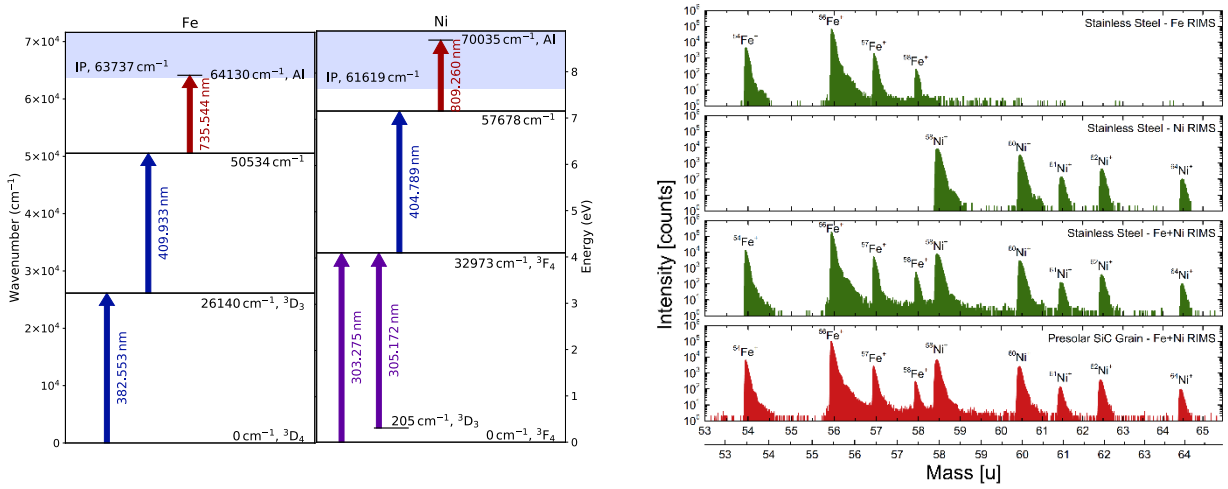


Figure 12: Simultaneous measurement of Fe and Ni isotopes avoiding the isobaric overlap at mass 58. Left: Three-color RIS schemes for Fe (left) and Ni (right). Right, from top: RIMS spectrum from stainless steel with only Fe lasers, RIMS spectrum of with Ni lasers delayed 200 ns to offset $^{58}$Ni from $^{58}$Fe, RIMS spectrum with both sets of lasers, RIMS spectrum of a SiC stardust grain with both sets of lasers. From (Stephan, Trappitsch et al. 2016).

such grains are all consistent with the astrophysical *s*-process, in which the rate of neutron capture is slow compared to the $\beta^-$ decay rate of nuclei such as $^{97}$Ru (2.9 days) and $^{103}$Ru (39.3 days). Comparing the spectra from such grains to stellar models allows the determination of the size range and metallicity (i.e. the concentration of elements heavier than He) of the parent stars that produced them. In addition, the relatively high precision (1-2%) in the $^{99}$Ru/$^{100}$Ru isotope ratio allowed the determination of the amount of $^{99}$Tc produced by the stars, which subsequently decayed to $^{99}$Ru (Savina, Davis et al. 2004). RIMS analyses of this type were first performed in the 1990s, and are credited with providing the first direct, unambiguous evidence for the astrophysical *s*-process (Nicolussi, Davis et al. 1997).

## Multi-element analysis

With enough lasers, RIMS can analyze several elements simultaneously, even when those elements have isobars. For example, Fe and Ni both have isotopes with mass 58, yet they can be analyzed simultaneously in stardust grains using a ToF RIMS system by delaying the ionization of Ni with respect to Fe. Figure 12 shows the mass spectrum for such an analysis (Stephan, Trappitsch et al. 2016). The horizontal axis in the figure has two scales, the top scale is calibrated to the flight time of Fe while the bottom is calibrated to the flight time of Ni. To achieve this mass separation, the ionization lasers for Ni were delayed by 200 ns with respect to the ionization lasers of Fe. This results in a slight loss of total nickel signal due to the increased sputtered neutral cloud expansion (Figure 7), however since the Fe and Ni are detected simultaneously, the sample utilization efficiency is twice as high as it would be if the two elements were detected sequentially. This is important in small samples such as stardust grains, and allows for more information to be gained from each grain (Trappitsch, Stephan et al. 2018). Iron and Ni in stardust grains have far smaller isotopic anomalies than Ru, so maximizing the information from each grain is important in determining the grain histories.

The Fe / Ni system is an ideal test case for isobaric separation by delayed ionization since the isobaric interference is at the heaviest stable Fe and the lightest stable Ni isotope and the abundance

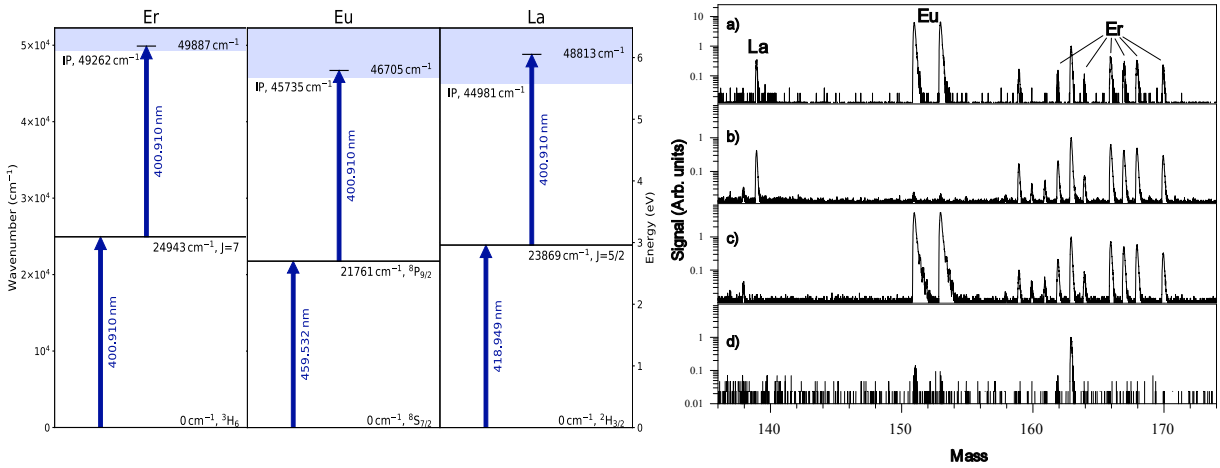


Figure 13: Left: Two-photon RIS schemes for La, Er, and Eu using a common ionization laser (400.910 nm) for all three elements. Right: a) RIMS spectrum with all lasers, b) Eu resonance laser blocked, c) La laser blocked, d) Er laser blocked.

of $^{58}$Fe is usually much lower than the abundance of $^{58}$Ni. To analyze two elements with multiple isobaric interferences simultaneously, peaks need to be shifted ideally by half masses as in Figure 12, which increases the mass resolution requirement, or by multiple masses in order to separate them completely. The latter method can, depending on the required delay time, result in a significantly lower detection limit for the delayed element due to reduced overlap of the neutrals with the ionization laser. The analyst must decide on a case-by-case basis if shifting the ToF spectrum of one element with respect to the other achieves the required result. In the case of atom-limited analysis, there may be no other way to do the measurement.

The RIMS spectrum in Figure 12 requires six tunable Ti:Sapphire lasers, three each for Fe and Ni, however it is possible to construct more economical two-color RIS schemes and reduce the number of lasers. For example, Sr, Zr, and Ba can be analyzed simultaneously using two lasers each (Stephan, Trappitsch et al. 2016). In this case there are no isobars, and so ionization is simultaneous. Where there are no isobars to separate, one can use a single laser to ionize all species (albeit with decreased efficiency since only one scheme will terminate on an autoionizing state) and reduce the total number of lasers further. Figure 13 shows RIS schemes and RIMS spectra for the simultaneous analysis for La, Eu, and Er, taken using laser desorption of a 50 μm chromatography bead containing $5\times10^{10}$ atoms each of five different lanthanides. Here the Er RIS scheme is one-color two-photon, with the same 400.91 nm photon both exciting and ionizing the Er atoms. In this case the scheme does not terminate on an autoionizing state, so it is not saturated. The 400.91 nm photon also ionizes the Eu and La (these are two-color two-photon RIS schemes), so that a total of three lasers suffices for all three elements.

The top panel of Figure 13 (spectrum a) is the RIMS spectrum obtained with all three lasers in use simultaneously, and shows that La, Eu, and Er are all detected. The relative ionization efficiencies and useful yields are undetermined since the laser desorption rates for the three elements under these conditions are not known. However, the signal-to-noise ratio is high even though the sample contains ~10 pg of each element, and the bead was not exhausted during the analysis.

The other three spectra in Figure 13 show the effects of blocking each of the lasers one at a time. Blocking the 459.562 nm laser (spectrum b) extinguishes the Eu signal while leaving the Er and La unchanged. Similarly, blocking the 418.849 nm laser (spectrum c) removes the La signal without affecting the Er and Eu. Finally, blocking the 400.910 nm laser (spectrum d) extinguishes all three elemental signals, and leaves the background. There is significant non-resonant interference in the Er region, especially at *m/z* 163. This is likely due to the organic ligands that fix the atoms on the bead. Organic molecules and fragments can be non-resonantly ionized by the lasers, which in this case are all in the blue region of the visible and thus have enough energy to affect two- or three-photon ionization of some organic species.

## Electronic processes during vaporization

When atoms leave solid surfaces either by sublimation, sputtering, or pulsed laser desorption, a significant fraction of the population may reside in one or more low-lying electronically excited states. A practical effect of this is that RIS schemes that originate on atomic ground states, such as those in Figure 3, will not ionize these excited atoms, and the useful yield will be lower than expected. From a practical standpoint, RIS schemes can be devised to improve the useful yield. Figure 14 shows a two-color RIS scheme for uranium that simultaneously accesses both the $^6L_6$ ground state and a populated $^5K_5$ state at 620 cm$^{-1}$. Using pulsed SNMS on clean uranium metal with a single laser tuned to the transition originating on the ground state (396.263 nm), the useful yield is 24%. Addition of a second laser tuned to the transition originating on the $^5K_5$ state (404.249 nm) improves the useful yield to 38% (Savina, Trappitsch et al. 2018).

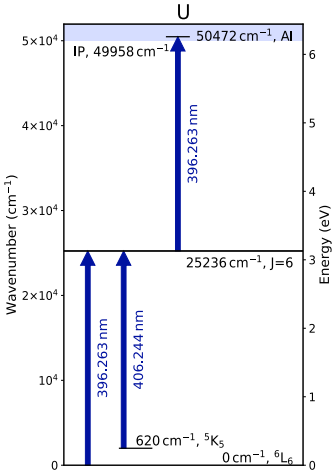


Figure 14: A two-color RIS scheme for uranium that accesses both the ground state and a sputter-populated low-lying excited state.

Beyond exploiting phenomenon for practical purposes, RIMS can be used to investigate the mechanisms by which sputtered or sublimated atoms receive electronic excitation from surfaces. The energies of observed low-lying states are often much too high to have been populated by a purely thermal mechanism. While there may be more than one process operating - for example the population of *J* states within a given multiplet often follows a thermal distribution - the dominant mechanism is likely resonant electron transfer (RET). In RET, electrons are transferred between the surface and the departing atom, with the atom and solid strongly coupled while the atom is still in the vicinity of the surface. As the separation increases the electronic states of the departing atom evolve from surface states to discrete atomic states. During this period, electrons are transferred between the atom and surface at rates that depend on the densities and occupations of surface states that best match the evolving atomic states (e.g. see Fig. 5 of ref. (Bastiaansen, Vervaecke et al. 2003)). The result is that atomic states whose wavefunctions are similar to populated surface states can have appreciable population.

Because RIMS can in principle be tuned to allowed transitions between any two states, the relative populations of states can be measured quantitatively and the predictions of theories such as RET can be tested. Furthermore, the delay time between the sputtering and ionization events

can be varied to produce velocity distributions of sputtered neutrals, since short delay times primarily sample fast atoms while long delay times sample slow atoms. This has consequences for RET, because faster atoms have shorter interaction times with the surface. Weakly coupled states in fast atoms will have a lower probability of being populated compared to slow atoms. This is demonstrated in RIMS analysis of Ni.

The ground state of Ni is $^3F_4$, however a $^3D_3$ state at 204.787 $cm^{-1}$ is significantly populated by sputtering or laser desorption. The top panel of Figure 15 shows that the populations of the ground and excited states are essentially equal upon ion sputtering. In fact, the Ni RIS scheme in Figure 12 originates on the $^3D_3$ state rather than the ground state. Density of states (DOS) calculations for metallic nickel predict predominantly D states near the Fermi level, accounting for the high population in both D and F states. Figure 15 plots state-selected velocity distributions obtained by RIMS and shows that the population of F states relative to D states drops off as the velocity of the departing atoms increases (Bastiaansen, Vervaecke et al. 2003). The bottom panel of Figure 15 shows that the relative populations of the D and F states in sputtered Ni atoms matches the RET prediction. The technique has been applied to a number of metals, with similar results (Vandeweert, Lievens et al. 2001, Bastiaansen, Philipsen et al. 2003, Bastiaansen, Vervaecke et al. 2003, Bastiaansen, Philipsen et al. 2004).

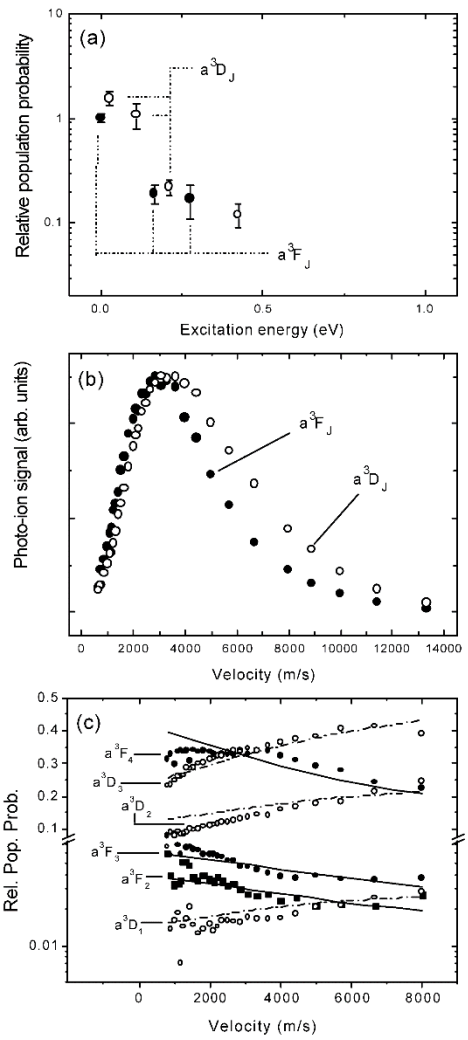


Figure 15: a) The relative populations of electronically excited D and F states of Ni atoms sputtered from a metallic surface. b) The RIMS signal from two D and F states as a function of the atom's departing velocity from the surface. c) A fit of the RET model to the state-selected velocity data. From (Bastiaansen, Vervaecke et al. 2003).

The influence of oxygen on the electronic structure of surfaces can also be studied in this way. Oxygen affects both the Fermi level and the local density of states. Partial oxidation of the surface increases the density of surface D states in the energy region near the ground state of departing Ni atoms. State-selected RIMS spectra show Ni atom population distributions shifting away from F states and toward D states as the surface oxidizes (Cortona, Husinsky et al. 1999). Further, the probability that an atom will sputter as a neutral rather than an ion is also affected by the strength and duration of the atom-surface coupling, since longer interaction time favor neutralization of departing ions. This is reflected in the state-selected velocity distributions for Ni atoms sputtered from metallic nickel and NiO; D states are favored in fast atoms much more so than F states when the surface is partially oxidized, showing the weakening of F-character in the surface.

## Resources

There are abundant resources available to aid in the construction of RIS schemes, and RIMS systems. Many of the fundamental principles of resonant photoionization (as well as other topics) are covered by Letokhov (Letokhov 1987). Review articles on RIMS are available in the literature (Payne, Deng et al. 1994, Wendt, Blaum et al. 1999, Wendt and Trautmann 2005). The US National Institute of Standards and Technology provides a wealth of atomic spectroscopic data useful for constructing RIS schemes. A searchable database on atomic levels and transitions, including level assignments and Einstein coefficients (where known) is available online (NIST 2019). A subset of this database including the most important and frequently used atomic spectroscopic data is available in the literature and is often a good place to start in the construction of a new RIS scheme, especially for first transitions (Sansonetti and Martin 2005). Saloman authored series of papers on RIS schemes for many elements, including published schemes and accompanying information from the NIST spectroscopic database (Saloman 1990, Saloman 1991, Saloman 1992, Saloman 1993, Saloman 1994). Laboratoire Aimé Cotton maintains an extensive online database for actinides including level assignments, line strengths, and isotope shifts (Blaise and Wyart 2019). The Resonance Ionization Laser Ion Source (RILIS) laboratory at the European Organization for Nuclear Research (CERN) uses resonance ionization to generate high-purity ion beams for use in nuclear physics research and hosts a user-generated database of RIS schemes (RILIS 2019). The RILIS group in collaboration with others authored a review article on the use of resonance ionization for nuclear physics that includes published RIS schemes for 51 elements (Fedosseev, Yu et al. 2012). In addition, a detailed discussion of the RILIS facility covering many basic aspects of resonance ionization is available (Marsh 2012).

## References

Bastiaansen, J., V. Philipsen, P. Lievens, R. E. Silverans and E. Vandeweert (2004). "Influence of the atomic structure on the quantum state of sputtered Ir atoms." Physical Review A **70**(5): 052902.

Bastiaansen, J., V. Philipsen, F. Vervaecke, E. Vandeweert, P. Lievens and R. E. Silverans (2003). "Velocity dependent electron transfer during emission of ion-beam sputtered Cu atoms." Physical Review B **68**(7): 073409.

Bastiaansen, J., F. Vervaecke, E. Vandeweert, P. Lievens and R. E. Silverans (2003). "Electronic processes during the sputtering of atoms from metallic surfaces studied by resonance laser ionization spectroscopy." Spectrochimica Acta Part B-Atomic Spectroscopy **58**(6): 1147-1154.

Bastiaansen, J., F. Vervaecke, E. Vandeweert, P. Lievens and R. E. Silverans (2003). "Modeling the multichannel electron transfer during the sputtering of Co atoms." Nuclear Instruments and Methods in Physics Research Section B: Beam Interactions with Materials and Atoms **203**: 158-163.

Blaise, J. and J.-F. Wyart. (2019). "Selected Constants, Energy Levels and Atomic Spectra of Actinides." 2017, from http://web2.lac.u-psud.fr/lac/Database/Contents.html.

Blaum, K., C. Geppert, W. Schreiber, J. Hengstler, P. Müller, W. Nörtershäuser, K. Wendt and B. Bushaw (2002). "Trace determination of gadolinium in biomedical samples by diode laser-based multi-step resonance ionization mass spectrometry." Analytical and Bioanalytical Chemistry **372**(7): 759-765.

Burbidge, E. M., G. R. Burbidge, W. A. Fowler and H. F. (1957). "Synthesis of the Elements in Stars." Reviews of Modern Physics **29**: 547-650.

Bushaw, B. A. and B. D. Cannon (1997). "Diode laser based resonance ionization mass spectrometric measurement of strontium-90." Spectrochimica Acta Part B: Atomic Spectroscopy **52**(12): 1839-1854.

Cortona, A., W. Husinsky and G. Betz (1999). "Influence of adsorbates, crystal structure, and target temperature on the sputtering yield and kinetic-energy distribution of excited Ni atoms." Physical Review B **59**(23): 15495-15505.

Crowther, S. A., R. K. Mohapatra, G. Turner, D. J. Blagburn, K. Kehm and J. D. Gilmour (2008). "Characteristics and applications of RELAX, an ultrasensitive resonance ionization mass spectrometer for xenon." Journal of Analytical Atomic Spectrometry **23**(7): 938-947.

Denk, E., D. Hillegonds, J. Vogel, A. Synal, C. Geppert, K. Wendt, K. Fattinger, C. Hennessy, M. Berglund, R. F. Hurrell and T. Walczyk (2006). "Labeling the human skeleton with 41Ca to assess changes in bone calcium metabolism." Analytical and Bioanalytical Chemistry **386**(6): 1587-1602.

Donohue, D. L., J. P. Young and D. H. Smith (1985). "Spectral Studies of Actinide Elements by Resonance Ionization Mass-Spectrometry." Applied Spectroscopy **39**(1): 93-97.

Eichler, B., S. Hübener, N. Erdmann, K. Eberhardt, H. Funk, G. Herrmann, S. Köhler, N. Trautmann, G. Passler and F.-J. Urban (1997). "An Atomic Beam Source for Actinide Elements: Concept and Realization." Radiochimica Acta **79**: 221-223.

Fedosseev, V. N., K. Yu and V. I. Mishin (2012). "Resonance laser ionization of atoms for nuclear physics." Physica Scripta **85**(5): 058104.

Franzmann, M., H. Bosco, L. Hamann, C. Walther and K. Wendt (2018). "Resonant laser-SNMS for spatially resolved and element selective ultra-trace analysis of radionuclides." Journal of Analytical Atomic Spectrometry **33**(5): 730-737.

Geppert, C., P. Müller, K. Wendt, C. Schnabel, H. A. Synal, U. Herpers and S. Merchel (2005). "Intercomparison measurements between accelerator and laser based mass spectrometry for ultra-trace determination of 41Ca in the 10−11–10−10 isotopic range." Nuclear Instruments and Methods in Physics Research Section B: Beam Interactions with Materials and Atoms **229**(3): 519-526.

Gilabert, E., B. Lavielle, B. Thomas, S. Topin, F. Pointurier and C. Moulin (2016). "Ultratrace analysis of krypton isotopes by resonant ionization spectroscopy-time of flight mass spectrometry (RIS-TOF)." Journal of Analytical Atomic Spectrometry **31**(4): 994-1001.

Gnaser, H. (1999). Low-energy ion irradiation of solid surfaces, Springer-Verlag.

Hervig, R. L., F. K. Mazdab, P. Williams, Y. Guan, G. R. Huss and L. A. Leshin (2006). "Useful ion yields for Cameca IMS 3f and 6f SIMS: Limits on quantitative analysis." Chemical Geology **227**(1-2): 83-99.

Hilborn, R. C. (1982). "Einstein coefficients, cross sections, f values, dipole moments, and all that." American Journal of Physics **50**(11): 982-986.

Isselhardt, B. H., M. R. Savina, K. B. Knight, M. J. Pellin, I. D. Hutcheon and S. G. Prussin (2011). "Improving Precision in RIMS: The Influence of Bandwidth in Uranium Isotope Ratio Measurements." Analytical Chemistry **83**: 2469-2475.

Iwata, Y., C. Ito, H. Harano and T. Iguchi (2014). "Performance evaluation of a resonance ionization mass spectrometer developed for the FFDL system of fast reactors." Journal of Nuclear Science and Technology **51**(4): 465-475.

Kron, T., Y. Liu, S. Richter, F. Schneider and K. Wendt (2016). "High efficiency resonance ionization of palladium with Ti:sapphire lasers." Journal of Physics B: Atomic, Molecular and Optical Physics **49**(18): 185003.

Letokhov, V. S. (1987). Laser photoionization spectroscopy, Academic Press.

Littman, M. G., M. M. Kash and D. Kleppner (1978). "Field-Ionization Processes in Excited Atoms." Physical Review Letters **41**(2): 103-107.

Liu, Y., C. Baktash, J. R. Beene, H. Z. Bilheux, C. C. Havener, H. F. Krause, D. R. Schultz, D. W. Stracener, C. R. Vane, K. Brück, C. Geppert, T. Kessler and K. Wendt (2006). "Laser ion source tests at the HRIBF on stable Sn, Ge and Ni isotopes." Nuclear Instruments and Methods in Physics Research Section B: Beam Interactions with Materials and Atoms **243**(2): 442-452.

Marsh, B. A. (2012). Resonance Ionization Laser Ion Sources. CAS-CERN Accelerator School: Ion Sources. R. Bailey. CERN, CERN**:** 203-263.

Nicolussi, G. K., A. M. Davis, M. J. Pellin, R. S. Lewis, R. N. Clayton and S. Amari (1997). "s-Process zirconium in presolar silicon carbide grains." Science **277**(5330): 1281-1283.

Nicolussi, G. K., M. J. Pellin, R. S. Lewis, A. M. Davis, S. Amari and R. N. Clayton (1998). "Molybdenum isotopic composition of individual presolar silicon carbide grains from the Murchison meteorite." Geochim. Cosmochim. Acta **62**(6): 1093-1104.

Niki, H., K. Motoki, M. Yasui, Y. Horiuchi, S. Tokita and Y. Izawa (2006). "Selectivity and Efficiency of Laser Isotope Separation Processes of Gadolinium." Journal of Nuclear Science and Technology **43**(4): 427-431.

NIST. (2019). "Atomic Spectra Database ", 2019, from https://physics.nist.gov/PhysRefData/ASD/levels_form.html.

Ofan, A., I. Ahmad, J. P. Greene, M. Paul and M. R. Savina (2006). "Development of a detection method for $^{244}$Pu by Resonance Ionization Mass Spectrometry." New Astronomy Reviews **50**(7-8): 640-643.

Palmer, B. A., R. A. Keller and R. J. Englemann (1980). An Atlas of Uranium Emission Intensities in A Hollow Cathode Discharge, Los Alamos National Laboratory**:** 240.

Payne, M. G., L. Deng and N. Thonnard (1994). "APPLICATIONS OF RESONANCE IONIZATION MASS-SPECTROMETRY." Review of Scientific Instruments **65**(8): 2433-2459.

Raeder, S., A. Hakimi, N. Stöbener, N. Trautmann and K. Wendt (2012). "Detection of plutonium isotopes at lowest quantities using in-source resonance ionization mass spectrometry." Analytical and Bioanalytical Chemistry **404**(8): 2163-2172.

Ranebo, Y., P. M. L. Hedberg, M. J. Whitehouse, K. Ingeneri and S. Littmann (2009). "Improved isotopic SIMS measurements of uranium particles for nuclear safeguard purposes." Journal of Analytical Atomic Spectrometry **24**(3): 277-287.

RILIS. (2019). "RILIS Elements." from http://rilis.web.cern.ch/elements.

Saloman, E. B. (1990). "A resonance ionization spectroscopy/resonance ionization mass spectrometry data service. I—Data sheets for As, B, Cd, C, Ge, Au, Fe, Pb, Si and Zn." Spectrochimica Acta Part B: Atomic Spectroscopy **45**(1): 37-83.

Saloman, E. B. (1991). "A resonance-ionization spectroscopy/resonance-ionization mass spectrometry data service. II. Data sheets for aluminum, calcium, cesium, chromium, cobalt, copper, krypton, magnesium, mercury, and nickel." Spectrochimica Acta, Part B: Atomic Spectroscopy **46B**(3): 319-378.

Saloman, E. B. (1992). "A resonance ionization spectroscopy/resonance ionization mass spectrometry data service: III—Data sheets for Sb, Bi, P, Na and Sn." Spectrochimica Acta Part B: Atomic Spectroscopy **47**(4): 517-543.

Saloman, E. B. (1993). "A resonance ionization spectroscopy/resonance ionization mass spectrometry data service: IV—Data sheets for Be, In, Li, K, Rb, Ag, Ti and V and an update of the data sheet for Ni." Spectrochimica Acta Part B: Atomic Spectroscopy **48**(9): 1139-1203.

Saloman, E. B. (1994). "A resonance ionization spectroscopy/resonance ionization mass spectrometry data service. V-Data sheets for Ga, Mn, Sc and Tl." Spectrochim. Acta, Part B **49B**(3): 251-281.

Sansonetti, J. E. and W. C. Martin (2005). "Handbook of Basic Atomic Spectroscopic Data." Journal of Physical Chemistry Reference Data **34**(4): 1559-2259.

Savina, M., A. M. Davis, C. E. Tripa, M. Pellin, R. S. Lewis, S. Amari and R. Gallino (2004). "Extinct Technetium in Silicon Carbide Stardust Grains: Implications for Stellar Nucleosynthesis." Science **303**: 649-652.

Savina, M. R., B. H. Isselhardt, A. Kucher, R. Trappitsch, B. V. King, D. Ruddle, R. Gopal and I. Hutcheon (2017). "High Useful Yield and Isotopic Analysis of Uranium by Resonance Ionization Mass Spectrometry." Analytical Chemistry **89**: 6224-6231.

Savina, M. R., M. J. Pellin, C. E. Tripa, I. V. Veryovkin, W. F. Calaway and A. M. Davis (2003). "Analyzing individual presolar grains with CHARISMA." Geochim. Cosmochim. Acta **67**(17): 3215-3225.

Savina, M. R., R. Trappitsch, A. Kucher and B. H. Isselhardt (2018). "New Resonance Ionization Mass Spectrometry Scheme for Improved Uranium Analysis." Analytical Chemistry **90**(17): 10551-10558.

Schumann, P. G., K. D. A. Wendt and B. A. Bushaw (2005). "High-resolution triple-resonance autoionization of uranium isotopes." Spectrochimica Acta Part B: Atomic Spectroscopy **60**(11): 1402-1411.

Smentkowski, V. S. (2000). "Trends in sputtering." Progress in Surface Science **64**(1–2): 1-58.

Stephan, T., R. Trappitsch, A. M. Davis, M. J. Pellin, D. Rost, M. R. Savina, R. Yokochi and N. Liu (2016). "CHILI – the Chicago Instrument for Laser Ionization – a new tool for isotope measurements in cosmochemistry." International Journal of Mass Spectrometry **407**: 1-15.

Stern, R. C. and B. B. Snavely (1976). "The Laser Isotope Separation Program at Lawrence Livermore National Laboratory." Annals of the New York Academy of Sciences **267**: 71-80.

Strashnov, I. and J. D. Gilmour (2014). "Resonance ionisation mass spectrometry of krypton and its applications in planetary science." Hyperfine Interactions **227**(1): 259-270.

Trappitsch, R., M. R. Savina and B. H. Isselhardt (2018). "Resonance Ionization of Titanium: High Useful Yield and New Autoionizing States." Journal of Analytical Atomic Spectrometry **33**: 1962.

Trappitsch, R., T. Stephan, M. R. Savina, A. M. Davis, M. J. Pellin, D. Rost, F. Gyngard, R. Gallino, S. Bisterzo, S. Cristallo and N. Dauphas (2018). "Simultaneous iron and nickel isotopic analyses of presolar silicon carbide grains." Geochimica et Cosmochimica Acta **221**(Supplement C): 87-108.

Trautmann, N. and K. Wendt (2012). Fast chemical separations and laser mass spectrometry – tools for nuclear research. Radiochimica Acta. **100:** 675.

Vandeweert, E., P. Lievens, V. Philipsen, J. Bastiaansen and R. E. Silverans (2001). "Measurements of the population partitions and state-selected flight-time distributions of keV ion-beam-sputtered metastable atoms." Physical Review B **64**(19): 195417.

Veryovkin, I. V., W. F. Calaway and M. J. Pellin (2004). "Calculating time-of-flight spectra of post-ionized sputtered neutrals." Nuclear Instruments and Methods in Physics Research B **219**: 1051-1057.

Veryovkin, I. V., W. F. Calaway and M. J. Pellin (2004). "Ion optics of a new time-of-flight mass spectrometer for quantitative surface analysis." Nuclear Instruments and Methods in Physics Research A **519**: 353-362.

Wallner, A., T. Faestermann, J. Feige, C. Feldstein, K. Knie, G. Korschinek, W. Kutschera, A. Ofan, M. Paul, F. Quinto, G. Rugel and P. Steier (2015). "Abundance of live 244Pu in deep-sea reservoirs on Earth points to rarity of actinide nucleosynthesis." Nat Commun **6**.

Wendt, K., K. Blaum, B. A. Bushaw, C. Grüning, R. Horn, G. Huber, J. V. Kratz, P. Kunz, P. Müller, W. Nörtershäuser, M. Nunnemann, G. Passler, A. Schmitt, N. Trautmann and A. Waldek (1999). "Recent developments in and applications of resonance ionization mass spectrometry." Fresenius' Journal of Analytical Chemistry **364**(5): 471.

Wendt, K. and N. Trautmann (2005). "Recent developments in isotope ratio measurements by resonance ionization mass spectrometry." International Journal of Mass Spectrometry **242**(2-3): 161.

Wucher, A. (2013). Laser post-ionisation - fundamentals. TOF-SIMS: Surface Analysis by Mass Spectrometry. J. C. Vickerman and D. Briggs, IM Publications.

Wunderlich, R. K., I. D. Hutcheon, G. J. Wasserburg and G. A. Blake (1992). "Laser-induced isotopic selectivity in the resonance ionization of osmium." Int. J. Mass Spectrom. Ion Processes **115**(2-3): 123-155.

Young, J. P., D. L. Donohue and D. H. Smith (1989). "Application of resonance ionization mass spectrometry to the lanthanide elements in the wavelength region of 430–455 nm." Spectrochimica Acta Part B: Atomic Spectroscopy **44**(2): 147-153.

Ziegler, S. L. and B. A. Bushaw (2008). "Ultratrace Uranium Fingerprinting with Isotope Selective Laser Ionization Spectrometry." Analytical Chemistry **80**: 6029-6033.